



Universiteit
Leiden
The Netherlands

Deep Spitzer/IRAC data for $z \approx 10$ galaxies reveal blue balmer break colors: young stellar populations at 500 Myr of cosmic time

Stefanon, M.; Bouwens, R.J.; Labbé, I.; Illingworth, G.D.; Gonzalez, V.; Oesch, P.A.

Citation

Stefanon, M., Bouwens, R. J., Labbé, I., Illingworth, G. D., Gonzalez, V., & Oesch, P. A. (2023). Deep Spitzer/IRAC data for $z \approx 10$ galaxies reveal blue balmer break colors: young stellar populations at 500 Myr of cosmic time. *The Astrophysical Journal*, 943(2).
doi:10.3847/1538-4357/aca470

Version: Publisher's Version

License: [Creative Commons CC BY 4.0 license](https://creativecommons.org/licenses/by/4.0/)

Downloaded from: <https://hdl.handle.net/1887/3715319>

Note: To cite this publication please use the final published version (if applicable).



Deep Spitzer/IRAC Data for $z \sim 10$ Galaxies Reveal Blue Balmer Break Colors: Young Stellar Populations at ~ 500 Myr of Cosmic Time

Mauro Stefanon^{1,2,3} , Rychard J. Bouwens³ , Ivo Labbé⁴ , Garth D. Illingworth⁵ , Valentino Gonzalez^{6,7} , and Pascal A. Oesch^{8,9}

¹ Departament d’Astronomia i Astrofísica, Universitat de València, C. Dr. Moliner 50, E-46100 Burjassot, València, Spain; mauro.stefanon@uv.es

² Unidad Asociada CSIC “Grupo de Astrofísica Extragaláctica y Cosmología” (Instituto de Física de Cantabria—Universitat de València), Spain

³ Leiden Observatory, Leiden University, NL-2300 RA Leiden, Netherlands

⁴ Centre for Astrophysics and SuperComputing, Swinburne, University of Technology, Hawthorn, VIC, 3122, Australia

⁵ UCO/Lick Observatory, University of California, Santa Cruz, 1156 High Street, Santa Cruz, CA 95064, USA

⁶ Departamento de Astronomía, Universidad de Chile, Casilla 36-D, Santiago 7591245, Chile

⁷ Centro de Astrofísica y Tecnologías Afines (CATA), Camino del Observatorio 1515, Las Condes, Santiago 7591245, Chile

⁸ Departement d’Astronomie, Université de Genève, 51 Ch. des Maillettes, CH-1290 Versoix, Switzerland

⁹ Cosmic Dawn Center (DAWN), Niels Bohr Institute, University of Copenhagen, Jagtvej 128, København N, DK-2200, Denmark

Received 2022 June 26; revised 2022 October 29; accepted 2022 November 18; published 2023 January 27

Abstract

We present the deepest constraints yet on the median rest-UV+optical spectral energy distribution (SED) of $z \sim 10$ galaxies prior to James Webb Space Telescope science operations. We constructed stacks based on four robust J_{125} dropouts, previously identified across the GOODS fields. We used archival Hubble Space Telescope/Wide Field Camera 3 data and the full-depth Spitzer/IRAC mosaics from the GREATS program, the deepest coverage at $\sim 3\text{--}5\ \mu\text{m}$ to date. The most remarkable feature of the SED is a blue IRAC $[3.6]\text{--}[4.5] = -0.18 \pm 0.25$ mag color. We also find a nearly flat $H_{160} - [3.6] = 0.07 \pm 0.22$ mag color, corresponding to a UV slope $\beta = -1.92 \pm 0.25$. This is consistent with previous studies and indicative of minimal dust absorption. The observed blue IRAC color and SED fitting suggest that $z \sim 10$ galaxies have very young (few $\times 10$ Myr) stellar populations, with 80% of stars being formed in the last $\lesssim 160$ Myr (2σ). While an exciting result, the uncertainties on the SED are too large to allow us to place strong constraints on the presence of a nebular continuum in $z \sim 10$ galaxies (as might be suggested by the blue $[3.6]\text{--}[4.5] < 0$ mag color). The resulting sSFR is consistent with the specific accretion rate of dark matter halos, indicative of a star formation efficiency showing quite limited evolution at such early epochs.

Unified Astronomy Thesaurus concepts: High-redshift galaxies (734); Lyman-break galaxies (979); Galaxy masses (607); Galaxy ages (576)

1. Introduction

Understanding how efficiently stars formed out of the cold gas accreted through the potential wells of the hierarchical assembly of the dark matter halos is one of the most fundamental questions in modern astrophysics (e.g., Madau & Dickinson 2014).

Over the last decade, the sensitive and high spatial resolution data acquired by the Wide Field Camera 3 on board the Hubble Space Telescope (HST) have enabled the detection and analysis of the rest-frame UV light emitted by recently born massive O-B stars (e.g., Kennicutt 1998) up to $z \sim 10\text{--}12$ (Bouwens et al. 2013, 2015, 2019, 2022; Coe et al. 2013; Oesch et al. 2014, 2016, 2018; Bernard et al. 2016; Calvi et al. 2016; McLeod et al. 2016; Ishigaki et al. 2018; Morishita et al. 2018; Salmon et al. 2018, 2020; Lam et al. 2019; Strait et al. 2020; Finkelstein et al. 2022; see also Harikane et al. 2022 for $z \sim 12$ candidates identified from ground-based near-IR data). These studies resulted in fundamental constraints on the total budget of newly formed stars across $\gtrsim 13$ Gyr of lookback time (the so-called cosmic star formation rate density, CSFRD; e.g., Bouwens et al. 2008, 2015, 2016a, 2022; Oesch et al. 2014; Finkelstein et al. 2015a; McLeod et al. 2016; Ishigaki et al. 2018; Oesch et al. 2018; Bhatawdekar et al. 2019).

Nonetheless, the highly successful Spitzer/IRAC (Fazio et al. 2004) has provided the community with an invaluable probe into the rest-frame optical light for galaxies at $z > 4$, complementing the information in the rest-frame UV from HST. These data have unveiled a very active universe, where high equivalent width (EW; $> 500\text{--}1000\ \text{\AA}$) line emission from $[\text{O III}] + \text{H}\beta$ (Labbé et al. 2013; Smit et al. 2014; Castellano et al. 2017; De Barros et al. 2019; Stefanon et al. 2019, 2022b; Bowler et al. 2020; Strait et al. 2020, 2021; Endsley et al. 2021a) and $\text{H}\alpha$ (Bouwens et al. 2016b; Faisst et al. 2016, 2019; Mármol-Queraltó et al. 2016; Rasappu et al. 2016; Smit et al. 2016; Caputi et al. 2017; Harikane et al. 2018; Lam et al. 2019; Maseda et al. 2020; Stefanon et al. 2022a) are typical and allowed to probe the stellar masses of galaxies at $z \sim 4\text{--}9$ (Duncan et al. 2014; Grazian et al. 2015; Song et al. 2016; Bhatawdekar et al. 2019; Kikuchihara et al. 2020) up to $z \sim 10$ (Oesch et al. 2016; Stefanon et al. 2021a).

The enormous progress in constraining the CSFRD and stellar mass, however, has not yet resulted in a clear consensus on the star formation efficiency (SFE; i.e., the ratio between the stellar mass M_* and the mass of the host dark matter halo M_{halo} : $\text{SFE} \equiv M_*/M_{\text{halo}}$) in the early universe. For example, some studies report an $\sim 10\times$ higher abundance of galaxies at $6 < z < 10$ (e.g., Ellis et al. 2013; McLeod et al. 2016) than other determinations at similar redshifts (e.g., Oesch et al. 2014, 2018; Bouwens et al. 2015) and stellar populations with pronounced Balmer/4000 Å breaks (Hashimoto et al. 2018; Mawatari et al. 2020; Roberts-Borsani et al. 2020;



Original content from this work may be used under the terms of the [Creative Commons Attribution 4.0 licence](https://creativecommons.org/licenses/by/4.0/). Any further distribution of this work must maintain attribution to the author(s) and the title of the work, journal citation and DOI.

Tacchella et al. 2022a), qualitatively consistent with an SFE increasing with increasing redshifts at early epochs (e.g., Finkelstein et al. 2015b; Behroozi et al. 2019). However, a number of more recent determinations of the star formation rate (SFR) and stellar mass densities using the largest samples suggest that the baryonic assembly is consistent with the accretion of the dark matter halos (Oesch et al. 2018; Tacchella et al. 2018; Stefanon et al. 2021a). Clearly, the James Webb Space Telescope (JWST) will rather quickly establish if the latest results are the most likely (or not).

Interestingly, but perhaps not surprisingly, the current redshift frontier ($z \sim 9\text{--}12$) is where systematic differences in the stellar mass and stellar-to-halo mass ratio determinations are the most evident (see, e.g., Stefanon et al. 2021a). Again, in this context, JWST observations will provide much more extensive insights, but we have the opportunity to make a significant step forward on this important question with existing data.

Observationally, the M_*/L ratio (where M_* indicates the stellar mass, and L is the luminosity in a specific band) or, equivalently, the age of the stellar population is arguably one of the main ingredients required to constrain the stellar mass assembly of galaxies. The Balmer/4000 Å break, one of the main proxies for stellar population age determinations (e.g., Kauffmann et al. 2003), is probed by the IRAC 3.6 μm band for redshifts in the range $7.2 \lesssim z \lesssim 8.7$. At $z \sim 8.7$, the Balmer/4000 Å break starts to leave the IRAC 3.6 μm band, and by $z \sim 9.7$, it has completely shifted into the 4.5 μm band. The 4.5 μm band, instead, at $7.0 \lesssim z \lesssim 9.2$ intercepts the emission from the $[\text{O III}]\lambda\lambda 4959, 5007$ and $\text{H}\beta$ lines, while for $z \gtrsim 9.2$, it is largely free of the most prominent emission lines (e.g., Anders & Fritze-v. Alvensleben 2003).

Fortunately, we can constrain the Balmer/4000 Å break for $z \sim 10$ galaxies by leveraging Spitzer/IRAC observations. At these redshifts, the IRAC 3.6 μm band probes the rest-frame UV (~ 3300 Å rest-frame), while the 4.5 μm band lies just redward of the Balmer/4000 Å break. This observational configuration is particularly effective at constraining the strength of the Balmer/4000 Å break given the contiguity of the two IRAC bands. Moreover, at $z \lesssim 9$, the typical uncertainties in photometric redshifts ($\Delta z \sim 0.4$) can prevent one from distinguishing a genuine Balmer/4000 Å break from an emission line contributing the 4.5 μm band (see, e.g., Figure 5 in Stefanon et al. 2021a), leading to potential overestimates of the stellar age (e.g., Stark et al. 2013; Stefanon et al. 2021a; Topping et al. 2022). Instead, the larger shift to redder wavelengths and the absence of strong line emission just redward of the Balmer break make this possibility less likely for $z \sim 10$ sources.

Thus, given the value of $z \sim 10$ samples for constraining the star formation history (SFH), we focus on inferring the main stellar population parameters for a robust sample of star-forming galaxies at $z \sim 10$ (Oesch et al. 2018). In particular, we characterize the rest-frame optical light, complementing the previous study of Wilkins et al. (2016b) centered on the rest-frame UV light. We do so by stacking the very sensitive observations available with Spitzer/IRAC data over the GOODS fields (Giavalisco et al. 2004) from the GOODS Re-ionization Era wide Area Treasury from Spitzer (GREATS) and other programs (Stefanon et al. 2021b). GREATS combined all of the relevant IRAC data (>4200 hr cumulative in the 3.6 and 4.5 μm bands) acquired throughout the scientific life of Spitzer,

Table 1
Sample of $z \sim 10$ Star-forming Galaxies Adopted in This Work

ID	Redshift	M_{UV} (mag)	5 σ Sensitivities ^a	
			3.6 μm (nJy)	4.5 μm (nJy)
GN-z11	11.1 ± 0.1^b	−21.6	53	78
GN-z10-2	9.9 ± 0.3	−20.7	67	103
GS-z10-1	9.9 ± 0.5	−20.6	51	79
XDFJ-3811362435	$9.9^{+0.7}_{-0.6}$	−17.6	48	77
Excluded ^c				
GN-z10-3 ^d	8.78	−20.7	71	124
XDFJ-4023680031 ^e	9.7 ± 0.6	−17.4	49	79

Notes.

^a Nominal 5 σ sensitivities from the IRAC SENS-PET exposure time calculator adopting the coverage depths from the GREATS mosaics.

^b Spectroscopic redshift from Oesch et al. (2018). Jiang et al. (2021) found a spectroscopic redshift of 10.957 ± 0.001 for this source.

^c Sources in the GOODS fields listed in Oesch et al. (2018) or Bouwens et al. (2015) but excluded from our analysis.

^d This source appears as a bona fide J dropout in the selections of Oesch et al. (2014, 2018); however, given reports of $\text{Ly}\alpha$ emission from the source and its thus seeming to lie at $z = 8.78$ (Laporte et al. 2021), we exclude it from our stack results.

^e Removed from our sample given the significant residuals present in the IRAC data after subtraction of the neighboring sources.

providing us with the deepest available 3–5 μm observations prior to the start of JWST science operations.

A brief description of the layout of this paper is as follows. In Section 2, we introduce the adopted sample and describe the relevant data sets, while in Section 3, we summarize our stacking procedure and the configurations we adopted to infer the main physical parameters. The resulting median spectral energy distribution (SED) is presented in Section 4, while in Section 5, we discuss its implications in galaxy assembly in the early universe. We summarize our findings in Section 6.

Throughout this paper, we adopt $\Omega_M = 0.3$, $\Omega_\Lambda = 0.7$, and $H_0 = 70 \text{ km s}^{-1} \text{ Mpc}^{-1}$, consistent with the most recent estimates from Planck (Planck Collaboration et al. 2020). Magnitudes are given in the AB system (Oke & Gunn 1983), while our M_* and SFR measurements are expressed in terms of the Salpeter (1955) initial mass function (IMF). For brevity, we denote the HST F435W, F606W, F775W, F850LP, F105W, F125W, F140W, and F160W as B_{435} , V_{606} , i_{775} , z_{850} , Y_{105} , J_{125} , JH_{140} , and H_{160} , respectively.

2. Data

The initial $z \sim 10$ sample considered for this study is composed of the five candidate $z \sim 10$ Lyman-break galaxies identified as J_{125} dropouts by Oesch et al. (2013, 2014, 2016, 2018) and Bouwens et al. (2010, 2011a, 2015, 2016a) across CANDELS (Grogin et al. 2011; Koekemoer et al. 2011) GOODS-N, GOODS-S (Giavalisco et al. 2004), the ERS field (Windhorst et al. 2011), and the UDF/XDF (Beckwith et al. 2006; Ellis et al. 2013; Illingworth et al. 2013) with the HUDF09-1 and HUDF09-2 parallels (Bouwens et al. 2011b). We complemented this sample with GN-z11 (Oesch et al. 2016), a star-forming galaxy spectroscopically confirmed at $z_{\text{spec}} = 11.1$ (Oesch et al. 2016; see also Jiang et al. 2021). In Table 1, we list the sources considered for this study and the main properties of the imaging data sets. The HST mosaics are characterized by 5 σ depths of

≈ 27.5 mag in the V_{606} and I_{814} bands, ≈ 26.7 – 27.5 mag in Y_{105} , and ≈ 26.8 – 27.8 mag in the J_{125} and H_{160} bands. An essential aspect of our study is the availability of exquisitely deep coverage at 3 – $5\ \mu\text{m}$ in the GOODS fields from the Spitzer/IRAC GREATS program (PI: Labbé; Stefanon et al. 2021b). These mosaics combine all of the useful IRAC imaging data acquired during the >15 yr of Spitzer science operations, with typical 5σ depths of ≈ 26.0 – 27.0 mag in the IRAC 3.6 and $4.5\ \mu\text{m}$ bands.

Considering the typical uncertainties in photometric redshifts ($\Delta z \lesssim 0.6$), our $z \sim 10$ sample selection minimizes the potential contamination of line emission that could affect the $4.5\ \mu\text{m}$ band for $z \lesssim 9$ sources (see, e.g., Figure 5 of Stefanon et al. 2021a), increasing the robustness of the inferred physical properties.

To overcome the challenge posed by the broad Spitzer/IRAC point-spread function (PSF) and light from neighboring sources contaminating flux measurements at $>3\ \mu\text{m}$, we followed the procedure used in Stefanon et al. (2021a, 2022a, 2022b) and subtracted the light from neighboring sources with MOPHONGO (Labbé et al. 2006, 2010a, 2010b, 2013, 2015). A critical ingredient for this step was the availability of accurate location-dependent PSFs from GREATS, as the asymmetric profile of the instrumental IRAC PSF and the variety of programs included in the mosaics result in significant variation of the PSF light profile across the mosaics (see, e.g., Stefanon et al. 2021b). As a result of this process, one source (XDFJ-4023680031) was removed from our sample, as it showed residual contamination after visual inspection.

Finally, we removed GN-z10-3 to be conservative. While it was initially identified as having a redshift of $z \sim 10$ (Oesch et al. 2014), Laporte et al. (2021) reported the detection of a candidate $\text{Ly}\alpha$ line, suggesting that the redshift may be $z_{\text{Ly}\alpha} = 8.78$ (Laporte et al. 2021). Our analysis therefore was conducted without GN-z10-3 and on the remaining four sources (see Table 1).

3. Analysis

We applied our consolidated stacking procedure (Stefanon et al. 2022a, 2022b for details) to construct the median SED of $z \sim 10$ star-forming galaxies. We median-stacked the photometry in the HST bands normalized by the flux density in the H_{160} band of each source. Uncertainties associated with the flux densities were computed by bootstrapping the procedure 1000 times.¹⁰ The stacked flux density in the H_{160} band instead corresponds to the median of the individual photometric measurements, while the associated uncertainty was computed by bootstrapping the procedure 1000 times. For the IRAC 3.6 and $4.5\ \mu\text{m}$ bands, instead, we median-stacked the image stamps centered on each source after normalizing them by the corresponding H_{160} flux density. For this step, we combined the stamps obtained after removing the contribution of all neighboring sources within a radius of $9''$. The flux density in the stacked IRAC stamps was measured in apertures of $2''.5$ diameter and corrected to total flux densities using the median of the PSFs reconstructed at the location of each source (the applied correction factors are 1.85 and 1.91 for the 3.6 and $4.5\ \mu\text{m}$ bands, respectively). Uncertainties were computed by measuring the dispersion of the flux density estimates in $20\ 2''.5$

wide apertures randomly placed across the stacked stamp within $7''.5$ of the center and repeating the process $10\times$ to increase the statistical significance. Finally, all values were rescaled by the median of the flux density in the H_{160} band. These stacked images were then used in our stellar population analysis.

We estimated the main stellar population parameters using the Bayesian tool PROSPECTOR (Johnson et al. 2021), which runs on the FLEXIBLE STELLAR POPULATION SYNTHESIS (FSPS) package (Conroy & Wechsler 2009; Conroy & Gunn 2010) with the MODULES FOR EXPERIMENTS IN STELLAR ASTROPHYSICS ISOCRONES AND STELLAR TRACKS (MIST; Choi et al. 2016; Dotter 2016). Our estimates are based on a Salpeter (1955) IMF defined between 0.1 and $240\ M_{\odot}$, a Calzetti et al. (2000) extinction curve, a $Z_{\text{star}} \equiv Z_{\text{gas}} = 0.2\ Z_{\odot}$ metallicity, an ionization parameter $\log U = -2.5$ (e.g., Stark et al. 2017; De Barros et al. 2019), and a formation redshift of $z = 20$ (Hashimoto et al. 2018; Mawatari et al. 2020; Harikane et al. 2022; Tacchella et al. 2022a). In particular, the larger IMF upper mass cutoff can provide an intense ionizing field (and therefore strong nebular emission lines) to ages older than possible with a conventional Salpeter IMF defined over 0.1 – $100\ M_{\odot}$, mitigating potential biases in our stellar mass estimates. We note, however, that the stellar masses we compute from our stacked photometry adopting the conventional Salpeter IMF differ by just $\lesssim 0.04$ dex from those computed with the 0.1 – $240\ M_{\odot}$ IMF.

The FSPS templates adopted in our analysis include the effects of nebular emission (both continuum and lines). These were obtained by reprocessing the simple stellar population templates through CLOUDY (Ferland et al. 2013); we refer the reader to Byler et al. (2017) for full details on the adopted procedure and a detailed characterization of the results. To provide the reader with a sense of the intensities of the emission lines utilized in our analysis, the templates for the constant SFH (CSFH) corresponding to ages of 3, 30, and 300 Myr have rest-frame EW_0 for $[\text{O II}]_{\lambda 3727}$ of $\text{EW}_0([\text{O II}]_{\lambda 3727}) \sim 510, 170$, and $110\ \text{\AA}$, respectively (corresponding to $\sim 1.7\times, 1.8\times$, and $1.9\times$ the flux of $\text{H}\beta$); $\text{EW}_0(\text{H}\beta) \sim 590, 170$, and $80\ \text{\AA}$; $\text{EW}_0([\text{O III}]_{\lambda 4959}) \sim 890, 120$, and $110\ \text{\AA}$ ($\sim 1.4\times, 1.2\times$, and $1.3\times$ the flux of $\text{H}\beta$); and $\text{EW}_0([\text{O III}]_{\lambda 5007}) \sim 2700, 690$, and $330\ \text{\AA}$ ($\sim 4.3\times, 3.8\times$, and $3.9\times$ the flux of $\text{H}\beta$).

Given that recent studies indicate that parametric SFHs could be underestimating the masses at high redshifts (e.g., Leja et al. 2019b; Topping et al. 2022; Whitler et al. 2022), we considered two different SFHs: a CSFH and a nonparametric SFH. In particular, we assumed that the nonparametric SFH was defined by four bins in time measured backward starting from the cosmic time corresponding to $z = 9.9$, the redshift we assumed for our stack. Specifically, the four bins were fixed at 0–3, 3–13, 13–100, and 100–300 Myr, respectively, with a Student’s t -distribution continuity prior modulating the ratio of the SFR in contiguous bins with $\nu = 2$ and $\sigma = 2$ (see discussions in Leja et al. 2019a; Tacchella et al. 2022a). This configuration can concurrently accommodate a recent burst of star formation and significant star formation during the initial assembly of the galaxy (Hashimoto et al. 2018; Roberts-Borsani et al. 2020; Tacchella et al. 2022a; Whitler et al. 2022). We also repeated the process with up to eight bins in time (0–3, 3–13, and 13–100 Myr and log-spaced afterward), finding similar results.

Finally, we also considered a third model with a CSFH and pure stellar emission (i.e., assuming the nebular continuum and

¹⁰ We utilize 1000 iterations for our bootstrap procedure to accurately estimate the confidence interval for fractional array indexes. Moreover, we find that 1000 iterations provide robust confidence intervals irrespective of the actual sample size for sample sizes typical of these redshifts.

Table 2
Flux Densities for Our Median-stacked Photometry

	V_{606} (nJy)	i_{775} (nJy)	z_{850} (nJy)	Y_{105} (nJy)	J_{125} (nJy)	JH_{140} (nJy)	H_{160} (nJy)	$3.6\ \mu\text{m}$ (nJy)	$4.5\ \mu\text{m}$ (nJy)
Stack	-1.0 ± 5.8	-0.6 ± 8.3	-5.1 ± 11.6	-4.7 ± 7.1	14.7 ± 10.3	51.2 ± 22.3	71.2 ± 8.8	75.8 ± 12.5	64.3 ± 10.3

Note. We only list the flux densities in those bands available for at least 90% of the sources in our sample.

line emission are negligible). During the fits, the redshift was fixed to the median of the photometric redshifts of the sample (z_{median}). Instead, the SFR integrated over the cosmic time (i.e., the total mass M_T) and the dust optical depth at $5500\ \text{\AA}$ (τ_{5500}) varied under a flat prior ($6 \leq \log M_T/M_\odot \leq 11$ and $0 \leq \tau_{5500} \leq 5$, respectively). Nonetheless, the mass values quoted in this paper refer to the mass in surviving stars (i.e., stellar mass M_*), obtained by rescaling M_T by the estimated stellar-to-total mass ratio (the MFRAC parameter, with typical values in the range of ~ 0.8 – 1.0).

The SFRs were computed by converting the UV luminosity using the factors listed by Madau & Dickinson (2014), interpolated for a $Z=0.2\ Z_\odot$ metallicity and a Salpeter (1955) IMF. Because of the increasing indication of negligible dust emission at early epochs (e.g., Bouwens et al. 2016a, 2020; Dunlop et al. 2017; McLure et al. 2018) and considering the small A_V values obtained with the nonparametric and CSFH configurations (see Section 5), we opted for not correcting the SFR for dust extinction. We finally computed the specific SFR (sSFR; $\equiv \text{SFR}/M_*$) by combining the SFR and M_* values previously estimated.

4. Results

Table 2 lists the photometric measurements from our stacking procedure, while in Figure 1, we display the stacked stamps and the measured broadband SED. To further validate our stacking analysis, and as an initial guide to the interpretation of our results, in Figure 1, we also present the best-fitting template from EAZY (Brammer et al. 2008; see Stefanon et al. 2021a, 2022b for details on the template set we adopted with EAZY).

The most prominent feature consists of a blue $[3.6]$ – $[4.5] = -0.18 \pm 0.25$ mag color. Because at $z \sim 10$, the IRAC $3.6\ \mu\text{m}$ band probes the rest UV, while the $4.5\ \mu\text{m}$ band lies just redward of the Balmer/4000 \AA break, the $[3.6]$ – $[4.5]$ color brackets the Balmer/4000 \AA break, an indicator of stellar population age (e.g., Kauffmann et al. 2003). The measured blue color then suggests young stellar populations (e.g., Inoue 2011), either as the result of a very rapid assembly of stars (e.g., an exponentially rising SFH) or as a recent burst of star formation. We will return to the implications of the $[3.6]$ – $[4.5]$ color on the stellar populations at $z \sim 10$ in Section 5.2.

Our stacked SED is also characterized by an approximately flat H_{160} – $[3.6] = 0.07 \pm 0.22$ mag color, corresponding to a UV slope $\beta = -1.92 \pm 0.25$, marginally redder than but consistent with the previous estimates of $\beta = -2.1 \pm 0.3$ at $z \sim 10$ by Wilkins et al. (2016a). This result is not very surprising, considering that three-fourths of the sources in our sample are in common with that of Wilkins et al. (2016a). Our UV slope estimate is also consistent with the recent measurements for $z \sim 9$ sources by Bhatawdekar & Conselice (2021; $\beta = -2.1 \pm 0.4$ for $M_{\text{UV}} \sim -21$ mag) and Tacchella et al. (2022a; $\beta = -1.9 \pm 0.3$). It is reassuring to find consistent measurements considering that the

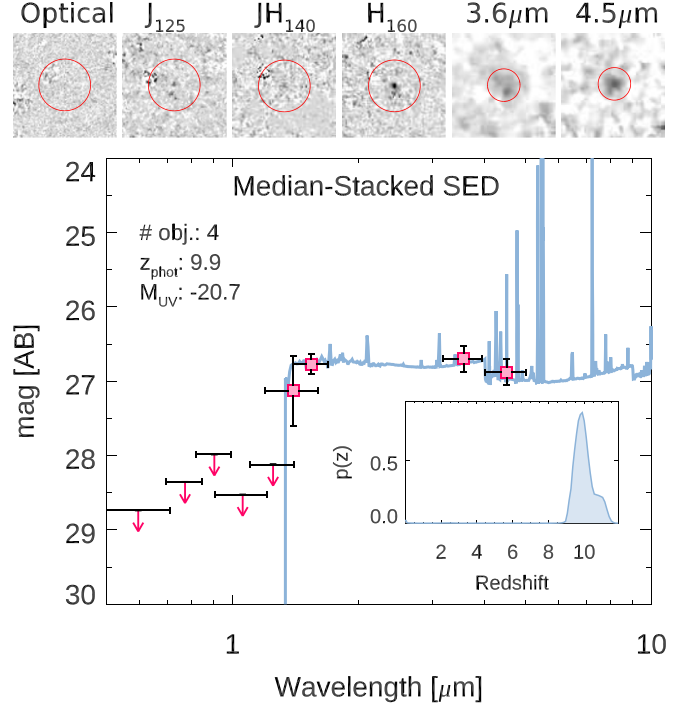


Figure 1. Top panels: stacked image stamps in the HST and IRAC bands, as labeled at the top, centered on the median stacks. The stamps for the HST bands are $5''.0$ side- 1 , while those in the IRAC bands are $8''.0$ wide. The HST optical stack combines all of the data available blueward of the J_{125} band (i.e., B_{435} , V_{606} , i_{775} , and z_{850}). The red circle marks the $2''.5$ diameter aperture adopted for our Spitzer/IRAC photometry. The HST stacks are shown for context, but we emphasize that our median HST flux measurements were derived from our photometry on individual sources. Bottom panel: median-stacked SED resulting from our analysis. The stacked photometry is presented both as red squares with 1σ errors and as red downward-pointing arrows indicating 2σ upper limits. The effective width of each band is marked by the black horizontal bar. The blue curve corresponds to the best-fitting EAZY template. The inset shows the redshift probability distribution computed by EAZY. Labels in the top left corner indicate the number of objects entering the stack, the median redshift, and the M_{UV} computed by EAZY (top to bottom). The SED is characterized by a blue IRAC $[3.6]$ – $[4.5]$ color, indicative of young stellar populations.

IRAC data adopted for this work (Stefanon et al. 2021b) have on average $\sim 2\times$ longer exposure times than the mosaics available to Wilkins et al. (2016a).

5. Discussion

Figure 2 displays the results of our template fitting analysis, while in Table 3, we list the values of the main physical parameters. In what follows, we adopt the results from the nonparametric SFH as reference.

5.1. Assessing the Potential Contribution of $[O\text{II}]$ Line Emission to the $3.6\ \mu\text{m}$ Flux Density

Before analyzing the physical implications of the measured blue $[3.6]$ – $[4.5]$ color, here we assess the robustness of this

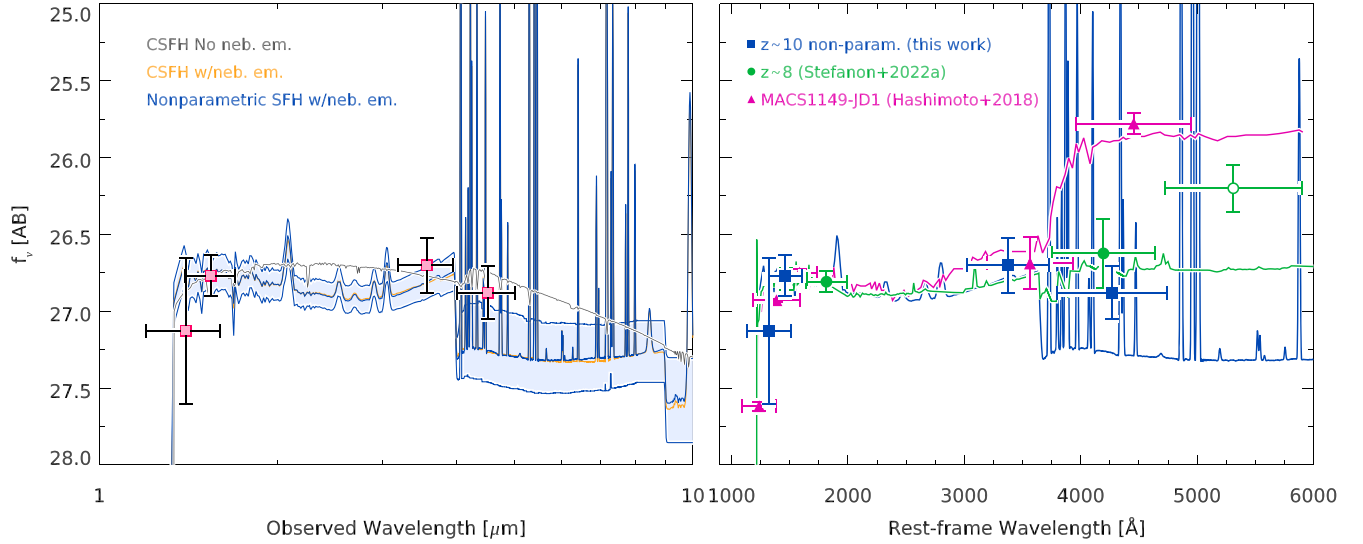


Figure 2. (Left) Best-fit SEDs resulting from the different configurations adopted in estimating the main stellar population parameters of our stack. In particular, we considered a CSFH model with and without nebular emission (orange and gray solid curves, respectively) and a nonparametric SFH (blue curve; see Section 3 for details), which we adopt as reference (the orange and blue curves are essentially indistinguishable). The shaded blue area corresponds to the SED posteriors marginalized over the 68% confidence interval for the nonparametric configuration. (Right) Comparison of our SED at $z \sim 10$ (filled blue squares and curve) with results from other studies. Specifically, we show the median SED at $z \sim 8$ corresponding to the $M_{UV} \sim -20.7$ mag bin from Stefanon et al. (2022b; green circles and curve) and the SED of MACS 1149-JD1 (Hashimoto et al. 2018; filled purple triangles and curve; here we adopt the photometric measurements of Zheng et al. 2017), a star-forming galaxy at $z_{spec} = 9.1$ characterized by an apparent pronounced Balmer break (Hashimoto et al. 2018). All wavelengths have been shifted to their rest frame. The photometric measurements and best-fit SEDs from Stefanon et al. (2022b), Hashimoto et al. (2018), and Zheng et al. (2017) have been renormalized to match the luminosity of our $z \sim 10$ stack at 1600 \AA . We removed the main emission lines from the SEDs of Stefanon et al. (2022b) and Hashimoto et al. (2018) to improve readability but note the likely substantial contribution of the $[O III]_{\lambda\lambda 4959,5007}$ doublet to the measured flux at $\lambda \sim 5200 \text{ \AA}$ for the Stefanon et al. (2022b) results (open green circle). Our stacked photometry can be better described by young stellar population templates, a result likely driven by the observed blue $[3.6] - [4.5] \lesssim 0$ mag color, consistent with the previous median determinations at $z \sim 8$ by Stefanon et al. (2022b).

Table 3
Main Stellar Population Parameters Inferred for Our Stacked SED

Property	Value		
z_{median}	9.9		
M_{UV}	-20.7 ± 0.1 mag		
UV slope β	-1.92 ± 0.25		
SFR _{UV} ^a	$9.1^{+0.9}_{-0.8} M_{\odot} \text{ yr}^{-1}$		
SFH	Nonparam.	CSFH	CSFH no neb.
$\log(t_{\ell,50}/\text{yr})^b$	$6.4^{+1.2}_{-0.2}$	$6.4^{+0.7}_{-0.4}$	$6.1^{+0.2}_{-0.4}$
$\log(t_{\ell,80}/\text{yr})^b$	$7.6^{+0.6}_{-1.2}$	$6.6^{+0.7}_{-0.4}$	$6.3^{+0.2}_{-0.4}$
$\log(M_{\star}/M_{\odot})$	$8.4^{+0.4}_{-0.2}$	$8.4^{+0.3}_{-0.1}$	$9.3^{+0.1}_{-0.4}$
A_V (mag)	$0.2^{+0.1}_{-0.1}$	$0.2^{+0.1}_{-0.1}$	$1.1^{+1.1}_{-0.6}$
sSFR (Gyr^{-1}) ^c	$33.4^{+24.1}_{-19.8}$	$40.0^{+27.5}_{-36.0}$	$4.6^{+5.9}_{-0.7}$ ^d

Notes. The measurements for $\log(t_{\ell,50}/\text{yr})$, $\log(t_{\ell,80}/\text{yr})$, $\log(M_{\star}/M_{\odot})$, A_V , and sSFR refer to the median and 16th–84th percentiles of the posteriors.

^a The SFR computed from the rest-frame UV luminosity and assuming negligible dust obscuration. We warn the reader that, given the high fraction of obscured star formation in the configuration without nebular emission (CSFH no neb.), the corresponding SFR_{UV} value is potentially underestimated. Assuming a Calzetti et al. (2000) curve, the unobscured+obscured SFR for this configuration would result in an $\approx 12\times$ larger value. This, however, is not the option that we consider to be most likely.

^b Lookback time encapsulating 50% and 80% ($\log(t_{\ell,50}/\text{yr})$ and $\log(t_{\ell,80}/\text{yr})$, respectively) of stellar mass assembly.

^c The sSFR obtained by dividing the unobscured SFR_{UV} by the stellar mass M_{\star} .

^d This value of sSFR does not account for the obscured fraction of SFR, and it is therefore likely underestimated in this case. A correction assuming a Calzetti et al. (2000) extinction curve would result in an $\approx 12\times$ larger value. Again, this is not the option that we consider to be the most likely.

estimate against potential contamination by major emission lines, in particular the impact of $[O II]_{\lambda 3727}$ on the $3.6 \mu\text{m}$ flux density.

The photometric redshift solutions for three sources in our sample allow for $z < 9.5$ at $\lesssim 1\sigma$ – 2σ (see Table 1). For $7.6 \lesssim z \lesssim 9.5$, the $3.6 \mu\text{m}$ band intercepts emission from $[O II]$. The $4.5 \mu\text{m}$ band is instead free from emission by the main nebular lines (e.g., Anders & Fritze-v. Alvensleben 2003) for $9.3 \lesssim z \lesssim 9.7$.¹¹ If these sources have redshifts $9.3 \lesssim z \lesssim 9.5$, emission from $[O II]$ could boost the $3.6 \mu\text{m}$ band flux density, resulting in apparent bluer $[3.6] - [4.5]$ colors and potentially younger stellar population ages.

We quantified the impact of $[O II]$ emission through the following Monte Carlo simulation. For each source, we randomly drew 10^4 redshift values from the corresponding $p(z)$ over the redshift range $7.0 \leq z \leq 9.5$ and computed the cumulative rest-frame EW₀ resulting from all of the emission lines intercepted by the $3.6 \mu\text{m}$ band at each redshift. Here we set the lower bound of the redshift range equal to $z = 7.0$ to be conservative. We adopted a rest-frame EW₀([O II]) = 200 \AA (corresponding to an ~ 0.25 mag excess in the $3.6 \mu\text{m}$ band flux density), consistent with values inferred from recent broadband photometric analyses at $z \sim 8$ (e.g., Stefanon et al. 2021b). We also adopted a flat f_{ν} SED and considered all of the emission lines listed in Anders & Fritze-v. Alvensleben (2003). We finally computed the EW of the relevant emission lines rescaling the EW₀([O II]) with the line ratios for subsolar metallicity.

When the three sources are considered individually, our simulation indicates small excesses of $0.0^{+0.05}_{-0.00}$, $0.0^{+0.26}_{-0.00}$, and

¹¹ At $z \sim 9.3$, emission from the $[O III]$ and $H\beta$ lines enters the $4.5 \mu\text{m}$ band.

$0.05^{+0.26}_{-0.05}$ mag for GN-z10-2, GN-z10-1, and XDFJ-3811362435, respectively, qualitatively consistent with the small probabilities we estimate for each object to be at $7.0 \leq z \leq 9.5$ (0.09, 0.21, and 0.28, respectively). Most importantly, the distribution of EW after median-combining the results from each run of the Monte Carlo simulation indicates an excess of just $0.00^{+0.06}_{-0.00}$ mag. We therefore conclude that the contribution of [O II] line emission has a negligible impact on the [3.6]–[4.5] color at $z \sim 10$, further supporting our stellar age estimates.

We finally note that recent preliminary spectra of $z \sim 8$ star-forming galaxies with JWST/NIRSpec indicate [O II] emission with $\text{EW}_0([\text{O II}]) \sim 10\text{--}40 \text{ \AA}$ (e.g., Brinchmann 2022; Curti et al. 2023; assuming for the continuum the photometric measurements reported by Tacchella et al. 2022b), much lower than our initial assumptions, suggesting that the already marginal excess inferred through our Monte Carlo simulation is likely an upper limit.

5.2. Which Are the Typical Stellar Population Ages at $\sim 500 \text{ Myr}$ of Cosmic Time?

Interestingly, inspection of the nonparametric SFH shows that $\sim 62\%$ of the stellar mass was created in a burst during the most recent 3 Myr, a fraction that only marginally ($< 0.5\%$) depends on the number of time bins adopted as a prior for the SFH (see Section 3). However, it also indicates that 80% of stars were formed in the last $\lesssim 160 \text{ Myr}$ (2σ), suggesting that sustained star formation could be happening at earlier phases of mass assembly.

The analysis assuming a CSFH and nebular emission results in an extremely young stellar population age, $\log(\text{age}/\text{yr}) = 6.7^{+0.6}_{-0.4}$. Remarkably, the corresponding best-fit SED and main stellar population parameters are very close ($\Delta \log M_\star \sim 0.08 \text{ dex}$, $\Delta A_V \sim 0.02 \text{ mag}$) to those obtained with the nonparametric SFH, increasing the overall confidence in this result. Interestingly, the M_T for the nonparametric SFH is $\sim 0.2 \text{ dex}$ larger than that for the CSFH, consistent with recent results (e.g., Tacchella et al. 2022a). Indeed, we find an $\sim 1 \text{ dex}$ larger value of $\log(t_{80}/\text{yr})$ for the nonparametric SFH, consistent with a scenario of considerable star formation at the beginning of mass assembly. Instead, different MFRAC values (0.78 and 1.0 for the nonparametric and CSFH, respectively) mitigate the 0.2 dex systematic difference, leading to similar M_\star estimates.

The measured blue [3.6] – [4.5] $\lesssim 0 \text{ mag}$ color might be seen as suggestive of a Balmer jump SED seen in very young stellar populations (e.g., Bica et al. 1994; Schaerer & de Barros 2009, 2010; Inoue 2011). However, the [3.6] – [4.5] $< 0 \text{ mag}$ color is not even significant at 1σ , and the result can also be fit (reduced $\chi^2 \sim 0.6$) by a very young stellar population ($\sim 10^{6.4} \text{ yr}$) with no nebular continuum and a modest amount of dust extinction ($A_V \sim 1.1 \text{ mag}$, leading to an $\sim 1 \text{ dex}$ larger stellar mass).

Atacama Large Millimeter/submillimeter Array (ALMA) results also provide additional insights in this context. The obscured SFR for XDFJ-3811362435 corresponding to $A_V = 1.1 \text{ mag}$ is $\text{SFR}_{\text{observed}} \approx 6 M_\odot \text{ yr}^{-1}$,¹² significantly below the 4σ threshold ($\sim 51 M_\odot \text{ yr}^{-1}$; e.g., Bouwens et al. 2020, after conversion to a Salpeter 1955 IMF) in the deep ALMA

continuum mapping of the XDF region (ASPECS; Walter et al. 2016; Decarli et al. 2019; see also Dunlop et al. 2017). This results in no effective help in removing the degeneracy between the different SED solutions. Similarly, the $\text{SFR}_{\text{observed}} \approx 90 M_\odot \text{ yr}^{-1}$ for the median SED lies below the detection threshold ($\approx 700 M_\odot \text{ yr}^{-1}$ at 4σ) of the wide-area coverage of GOODS-ALMA (Franco et al. 2018), suggesting that sensitivities similar to ASPECS would be required to ascertain the existence of brighter (but rarer) dusty sources. An even shallower coverage exists in the far-IR for GOODS-N (e.g., Dowell et al. 2014; Liu et al. 2018), limiting further considerations. Instead, and qualitatively, the strong [O III] + H β line emission in star-forming galaxies ($\text{EW} \gtrsim 500\text{--}1000 \text{ \AA}$) at $6 \lesssim z \lesssim 8$ (see Section 1 for references) supports a similar scenario with significant nebular continuum at $z \sim 10$, just $\sim 150 \text{ Myr}$ earlier than $z \sim 8$, consistent with both the nonparametric and CSFH configurations.

5.3. Comparison to Previous Studies

Our results are consistent with the average blue color and young stellar ages Stefanon et al. (2022b) found for star-forming galaxies at $z \sim 8$, with recent analyses of individual sources in samples at $z > 7$ (e.g., Strait et al. 2020; Topping et al. 2022), and with the blue colors and, albeit marginally older, the stellar population ages Whitler et al. (2022) found for a sample of galaxies at $z \lesssim 7$. Nonetheless, indications of red IRAC [3.6] – [4.5] $> 0 \text{ mag}$ colors, suggestive of the presence of a Balmer break and more evolved stellar populations, have been found for some individual sources at similar redshifts (e.g., Huang et al. 2016; Roberts-Borsani et al. 2016, 2022; Hashimoto et al. 2018; Strait et al. 2020; Laporte et al. 2021; Tacchella et al. 2022a).

One potential limitation of the current results at $z \sim 9$ consists of the small number of sources with spectroscopic confirmation (only four galaxies with $8.5 \leq z_{\text{spec}} \leq 9.5$ exist in the literature; Zitrin et al. 2015; Hashimoto et al. 2018; Laporte et al. 2021; Larson et al. 2022). The typical uncertainties from photometric redshifts at $z \sim 9$ generally do not enable us to ascertain whether the IRAC 4.5 μm band is probing exclusively the stellar + nebular continuum or if instead it is also intercepting the contribution from strong emission by [O III] + H β , making the interpretation of red [3.6] – [4.5] $> 0 \text{ mag}$ colors more uncertain.

Nonetheless, recent works have shown the existence of sources with $z_{\text{spec}} \gtrsim 9$ and red IRAC colors (Hashimoto et al. 2018; Laporte et al. 2021). MACS 1149-JD1 (Zheng et al. 2012; Hashimoto et al. 2018; Hoag et al. 2018), at $z_{\text{spec}} = 9.1$ (Hashimoto et al. 2018), is perhaps the most enigmatic representative of this category. Its exceptionally red [3.6] – [4.5] $\sim 0.9 \text{ mag}$ color, indicative of a pronounced Balmer break, clearly contrasts with the \sim blue [3.6] – [4.5] $\lesssim 0 \text{ mag}$ color we find in our study (see Figure 2). It is also worth noting that while spectroscopic redshifts are necessary to accurately establish which emission lines could be contributing to the flux densities in IRAC bands, they are not always sufficient to robustly segregate evolved from young stellar population ages for $z \lesssim 9$ sources (e.g., GN-z10-3; see Laporte et al. 2021 and Figure 2 of Topping et al. 2022). The medium-band JWST/NIRCam filters and JWST/NIRSpec observations will soon enable us to probe the rest-frame optical continuum in between the emission lines at high- z , providing key information to

¹² We assumed the IRX– β relation (where $\text{IRX} \equiv L_{\text{IR}}/L_{\text{UV}}$ is the infrared excess, with L_{IR} and L_{UV} the infrared and UV luminosities, respectively; e.g., Meurer et al. 1999) for a Calzetti et al. (2000) attenuation curve. This relationship was shifted to match an unattenuated $\beta = -3$, consistent with the intrinsic UV slope of the unattenuated best-fit SED template, resulting in $\text{IRX} \sim 10$ for $\beta = -3$. The SFR corresponding to L_{IR} was estimated by adopting the Kennicutt (1998) conversion.

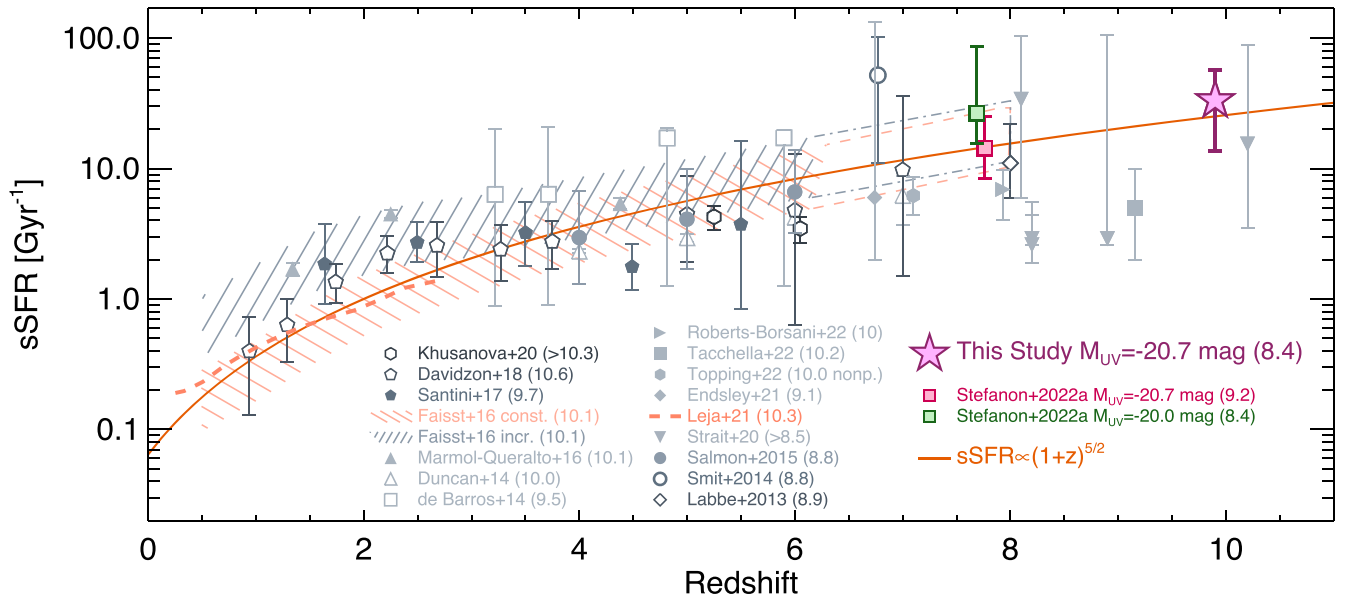


Figure 3. Evolution of the sSFR since $z \sim 10$. The estimate from this work (filled purple star) is presented together with determinations from the literature indicated by the legend. The number in parentheses indicates the $\log M_*$ for each set of measurements converted to a Salpeter (1955) IMF whenever necessary following the prescription of Madau & Dickinson (2014). The solid orange curve corresponds to the sSFR predicted by the strikingly simple model of Dekel et al. (2013), which builds on the assumption that the formation of stars in galaxies is dominated by the inflow of cold gas driven by the hierarchical merging of the dark matter halos. Our new measurement at $z \sim 10$ is consistent with the model prediction, suggesting marginal evolution in the SFE of galaxies with cosmic time. This supports previous findings at $z \sim 8$ (e.g., Stefanon et al. 2022b) and is indicative of minimal evolution in the SFE with cosmic time, beginning as early as just ~ 500 Myr after the Big Bang.

explore the ages and SFHs of the earliest generations of galaxies.

5.4. Evolution of the sSFR

In Figure 3, we display the sSFR value we computed from our stacked photometry adopting the nonparametric SFH (see Section 3 and Table 3). In the same figure, we also present previous determinations from the literature at $1 \lesssim z \lesssim 10$ (Labbé et al. 2013; Duncan et al. 2014; Smit et al. 2014; Salmon et al. 2015; Faisst et al. 2016; Mármol-Queralto et al. 2016; Santini et al. 2017; Davidzon et al. 2018; Khusanova et al. 2021; Strait et al. 2020; Endsley et al. 2021b; Leja et al. 2022; Roberts-Borsani et al. 2022; Tacchella et al. 2022a; Topping et al. 2022). To reduce the total density of data points shown at $z \sim 8-10$, the sSFR values for the studies of Endsley et al. (2021b), Topping et al. (2022), Tacchella et al. (2022a), and Roberts-Borsani et al. (2022) correspond to the median and 68% confidence interval we computed from the measurements presented in each study.

Our new determination is consistent with the measurements of Stefanon et al. (2022b) and Labbé et al. (2013) at $z \sim 8$ and at $\lesssim 2\sigma$ with those of Strait et al. (2020) at $z \gtrsim 8$ and the median for a sample at $z \sim 9$ analyzed by Tacchella et al. (2022a). Comparison of these measurements to those at lower redshifts suggests an sSFR monotonically growing with increasing redshift up to $z \sim 10$, albeit with a large ≈ 1 dex scatter.

Finally, to gather insights into the relationship between the hierarchical assembly of the dark matter halos and the stellar mass accretion of galaxies, in Figure 3, we also compare the measurements to the evolution of the sSFR predicted by Dekel et al. (2013). Briefly, through analytical considerations, Dekel et al. (2013) showed that the specific accretion rate of the dark matter halos in the extended Press–Schechter formalism (see also Neistein & Dekel 2008; Weinmann et al. 2011; Genel et al.

2014) can be written as $\dot{M}_h/M_h \simeq s M_{h,12}^\beta (1+z)^{2.5}$, M_h being the mass of the dark matter halo, $M_{h,12}$ the halo mass in units of $10^{12} M_\odot$, and s a mass-independent normalization factor. A value of $\beta = 0.14$ was found to well fit the merger trees from the Millennium simulation (Springel et al. 2005) with halo masses in the range $10^{11}-10^{14} M_\odot$ (Dekel et al. 2013). Given the already marginal dependence on the halo mass given by $\beta = 0.14$, we adopt the toy model of Dekel et al. (2013), which consists in setting $\beta = 0$. This removes any formal dependence of the evolution of the specific accretion rate of dark matter halos on the halo mass. The final values for the sSFR were obtained assuming that the baryonic accretion involved exclusively cold gas, corresponding to a time-independent conversion factor between the specific accretion rate of the dark matter halos and the sSFR. The agreement between our $z \sim 10$ estimate and the model prediction is quite remarkable, considering the minimal set of assumptions adopted in the Dekel et al. (2013) model. Stefanon et al. (2022b) found that galaxy assembly in the early universe was dominated by the accretion of dark matter halos and cold gas, with minimal evolution in the SFE. The determination of the sSFR to $z \sim 10$ from the present study extends that earlier result of an unevolving SFE by ~ 150 Myr to just ~ 500 Myr of cosmic time. In particular, this result qualitatively supports the unevolving stellar-to-halo mass ratio at $4 \lesssim z \lesssim 10$ inferred by Stefanon et al. (2021a) from the analysis of the stellar mass function of star-forming galaxies. This built on the work of Stefanon et al. (2017) using the evolution of the rest-frame optical luminosity function and Bouwens et al. (2015, 2021) based on the evolution in the UV luminosity function from $z \sim 10$ to zero. Interestingly, this is consistent with the predictions of recent models (e.g., Tacchella et al. 2018; Park et al. 2019).

Flux-limited samples could artificially introduce a trend of higher SFR toward higher redshifts. Our $z \sim 10$ sSFR estimate

could be particularly sensitive to this effect because the samples we adopted for our analysis were selected at rest-frame UV wavelengths, and our SFR was inferred from L_{UV} . However, because the sSFR is given by the ratio between the intrinsic (i.e., after correcting for the potential absorption effects by dust) SFR and M_* , lower SFR values alone are not sufficient to generate a lower sSFR. Instead, systems with larger M_*/L_{UV} ratios than found in our stack are necessary, i.e., galaxies either observed during a temporary state of low star formation or with evolved stellar populations.

Recent results indicate high duty cycle values for galaxies at intermediate and high redshifts, particularly at low masses (e.g., Faisst et al. 2019; Atek et al. 2022), suggesting that systems observed during a phase of reduced SFR should be rare in the early universe.

Interestingly, a number of studies report the existence of galaxies at $z \sim 7$ –11 with evolved stellar populations and/or $M_* > 10^{10} M_\odot$ (e.g., Hashimoto et al. 2018; Labbé et al. 2022), which results in low sSFR ~ 0.1 – 5 Gyr^{-1} (e.g., Hashimoto et al. 2018; Labbé et al. 2022). While these constitute exciting discoveries, the prevalence of galaxies at these redshifts and masses is still uncertain (e.g., Furlanetto & Mirocha 2022), creating a challenge for any efforts to statistically infer the impact that galaxies with reduced sSFR may have on the sSFR of the broad population of $z \sim 10$ galaxies.

Finally, heavy dust extinction ($A_V > 1 \text{ mag}$) could prevent us from further identifying evolved sources at these redshifts. Indeed, recent studies have revealed the existence of galaxies significantly affected by dust extinction at $3 \lesssim z \lesssim 8$, which are missed by conventional searches at rest UV (often referred to as HST-dark galaxies; e.g., Caputi et al. 2011; Stefanon et al. 2015; Wang et al. 2016, 2019; Alcalde Pampliega et al. 2019; Fudamoto et al. 2021; Barrufet et al. 2022). While these studies suggest that the HST-dark galaxies are preferentially found among massive systems (e.g., Wang et al. 2019; Barrufet et al. 2022), there is also an indication that these galaxies lie on the star-forming main sequence (e.g., Barrufet et al. 2022). We therefore conclude that the contribution of the HST-dark galaxies to our sSFR estimates should be quite small.

6. Conclusions

We derive the median SED of star-forming galaxies at $z \sim 10$, obtained by stacking the Spitzer/IRAC 3.6 and $4.5 \mu\text{m}$ image stamps, and the HST photometry of four robust J_{125} dropouts previously identified over the GOODS fields.

Crucial for our study are the deepest data at 3 – $5 \mu\text{m}$ before JWST starts its operations, provided by the GREATS program (PI: Labbé; Stefanon et al. 2021b), which at these redshifts bracket the Balmer/4000 Å break, a proxy for the age of the stellar population.

The most fascinating feature seen in the stacked SED is a blue $[3.6]$ – $[4.5] = -0.18 \pm 0.25 \text{ mag}$ color. At these redshifts, the $3.6 \mu\text{m}$ band probes the rest-frame UV, while the $4.5 \mu\text{m}$ band intercepts the rest-frame optical light. Given the wavelength contiguity of these two bands, the observed blue IRAC color suggests very young stellar populations. Indeed, a quantitative analysis through SED template fitting performed with PROSPECTOR (Leja et al. 2019a; Johnson et al. 2021) indicates that 80% of the stars assembled in the most recent $\lesssim 160 \text{ Myr}$ (2σ). The observed blue color contrasts with the red

$[3.6]$ – $[4.5]$ measurements for some sources in recent studies (e.g., MACS 1149-JD1; Hashimoto et al. 2018).


Finally, using the results from the SED fitting, we compute the sSFR. Our value is generally consistent with previous determinations at $z \lesssim 9$, although some estimates from the literature are only consistent at $\sim 2\sigma$. Overall, our analysis confirms the trend of a monotonic increase of the sSFR with increasing redshifts previously found for $z \lesssim 8$ (e.g., Faisst et al. 2016; Stefanon et al. 2022b). The sSFR measurements for $3 \lesssim z \lesssim 10$ are also broadly consistent with the toy model of Dekel et al. (2013), in which the formation of stars is dominated by the inflow of cold gas driven by the hierarchical merging of the dark matter halos.

This result, at $z \sim 10$, corresponding to just $\sim 500 \text{ Myr}$ of cosmic time, extends earlier results at $z \sim 8$ by Stefanon et al. (2022b) and indicates that galaxy assembly in the early universe was dominated by the accretion of dark matter halos and cold gas, with minimal evolution in the SFE.

Clearly, JWST science operations will provide completely game-changing insights into the stellar populations of galaxies and their prevalence earlier than 500 Myr of cosmic time thanks to the exquisite capabilities of JWST/NIRSpec, NIRCarn, and MIRI, facilitating a major leap in our understanding of galaxy formation. Our Hubble/Spitzer-driven result hints at exciting future insights from JWST’s study of the earliest galaxies.

The authors thank the referee for the competent and constructive report that improved the quality of the manuscript. M.S. acknowledges support from CIDEAGENT grant CIDEAGENT/2021/059 and project PID2019-109592GB-I00/AEI/10.13039/501100011033 from the Spanish Ministerio de Ciencia e Innovación—Agencia Estatal de Investigación. M.S. and R.J.B. acknowledge support from TOP grant TOP1.16.057. P.A.O. acknowledges support from the Swiss National Science Foundation through SNSF Professorship grant 190079 “Galaxy Build-up at Cosmic Dawn.” The Cosmic Dawn Center (DAWN) is funded by the Danish National Research Foundation under grant No. 140. We also acknowledge the support of NASA grants HSTAR-13252, HST-GO-13872, and HST-GO-13792 and NWO grant 600.065.140.11N211 (vrij competitie). G.D.I. acknowledges support for GREATS under RSA No. 1525754. V.G. gratefully acknowledges support by ANID BASAL projects ACE210002 and FB210003. This paper utilizes observations obtained with the NASA/ESA Hubble Space Telescope, retrieved from the Mikulski Archive for Space Telescopes (MAST) at the Space Telescope Science Institute (STScI). STScI is operated by the Association of Universities for Research in Astronomy, Inc., under NASA contract NAS 5-26555. This work is based in part on observations made with the Spitzer Space Telescope, which was operated by the Jet Propulsion Laboratory, California Institute of Technology, under a contract with NASA. Support for this work was provided by NASA through an award issued by JPL/Caltech.

ORCID iDs

Mauro Stefanon  <https://orcid.org/0000-0001-7768-5309>
 Rychard J. Bouwens  <https://orcid.org/0000-0002-4989-2471>
 Ivo Labbé  <https://orcid.org/0000-0002-2057-5376>
 Garth D. Illingworth  <https://orcid.org/0000-0002-8096-2837>

Valentino Gonzalez  <https://orcid.org/0000-0002-3120-0510>
 Pascal A. Oesch  <https://orcid.org/0000-0001-5851-6649>

References

- Alcalde Pampliega, B., Pérez-González, P. G., Barro, G., et al. 2019, *ApJ*, **876**, 135
- Anders, P., & Fritze-v. Alvensleben, U. 2003, *A&A*, **401**, 1063
- Atek, H., Furtak, L. J., Oesch, P., et al. 2022, *MNRAS*, **511**, 4464
- Barrufet, L., Oesch, P. A., Weibel, A., et al. 2022, arXiv:2207.14733
- Beckwith, S. V. W., Stiavelli, M., Koekemoer, A. M., et al. 2006, *AJ*, **132**, 1729
- Behroozi, P., Wechsler, R. H., Hearin, A. P., & Conroy, C. 2019, *MNRAS*, **488**, 3143
- Bernard, S. R., Carrasco, D., Trenti, M., et al. 2016, *ApJ*, **827**, 76
- Bhatawdekar, R., & Conselice, C. J. 2021, *ApJ*, **909**, 144
- Bhatawdekar, R., Conselice, C. J., Margalef-Bentabol, B., & Duncan, K. 2019, *MNRAS*, **486**, 3805
- Bica, E., Alloin, D., & Schmitt, H. R. 1994, *A&A*, **283**, 805
- Bouwens, R., González-López, J., Aravena, M., et al. 2020, *ApJ*, **902**, 112
- Bouwens, R. J., Illingworth, G. D., Franx, M., & Ford, H. 2008, *ApJ*, **686**, 230
- Bouwens, R. J., Illingworth, G. D., González, V., et al. 2010, *ApJ*, **725**, 1587
- Bouwens, R. J., Illingworth, G. D., Labbé, I., et al. 2011a, *Natur*, **469**, 504
- Bouwens, R. J., Illingworth, G. D., Oesch, P. A., et al. 2011b, *ApJ*, **737**, 90
- Bouwens, R. J., Illingworth, G. D., Oesch, P. A., et al. 2015, *ApJ*, **803**, 34
- Bouwens, R. J., Illingworth, G. D., van Dokkum, P. G., et al. 2022, *ApJ*, **927**, 81
- Bouwens, R. J., Oesch, P. A., Illingworth, G. D., et al. 2013, *ApJL*, **765**, L16
- Bouwens, R. J., Oesch, P. A., Labbé, I., et al. 2016a, *ApJ*, **830**, 67
- Bouwens, R. J., Oesch, P. A., Stefanon, M., et al. 2021, *AJ*, **162**, 47
- Bouwens, R. J., Smit, R., Labbé, I., et al. 2016b, *ApJ*, **831**, 176
- Bouwens, R. J., Stefanon, M., Oesch, P. A., et al. 2019, *ApJ*, **880**, 25
- Bowler, R. A. A., Jarvis, M. J., Dunlop, J. S., et al. 2020, *MNRAS*, **493**, 2059
- Brammer, G. B., van Dokkum, P. G., & Coppi, P. 2008, *ApJ*, **686**, 1503
- Brinchmann, J. 2022, arXiv:2208.07467
- Byler, N., Dalcanton, J. J., Conroy, C., & Johnson, B. D. 2017, *ApJ*, **840**, 44
- Calvi, V., Trenti, M., Stiavelli, M., et al. 2016, *ApJ*, **817**, 120
- Calzetti, D., Armus, L., Bohlin, R. C., et al. 2000, *ApJ*, **533**, 682
- Caputi, K. I., Cirasuolo, M., Dunlop, J. S., et al. 2011, *MNRAS*, **413**, 162
- Caputi, K. I., Deshmukh, S., Ashby, M. L. N., et al. 2017, *ApJ*, **849**, 45
- Castellano, M., Pentericci, L., Fontana, A., et al. 2017, *ApJ*, **839**, 73
- Choi, J., Dotter, A., Conroy, C., et al. 2016, *ApJ*, **823**, 102
- Coe, D., Zitrin, A., Carrasco, M., et al. 2013, *ApJ*, **762**, 32
- Conroy, C., & Gunn, J. E. 2010, *ApJ*, **712**, 833
- Conroy, C., & Wechsler, R. H. 2009, *ApJ*, **696**, 620
- Curti, M., D'Eugenio, F., Carniani, S., et al. 2023, *MNRAS*, **518**, 425
- Davidsen, I., Ilbert, O., Faisst, A. L., Sparre, M., & Capak, P. L. 2018, *ApJ*, **852**, 107
- De Barros, S., Oesch, P. A., Labbé, I., et al. 2019, *MNRAS*, **489**, 2355
- Decarli, R., Walter, F., González-López, J., et al. 2019, *ApJ*, **882**, 138
- Dekel, A., Zolotov, A., Tweed, D., et al. 2013, *MNRAS*, **435**, 999
- Dotter, A. 2016, *ApJS*, **222**, 8
- Dowell, C. D., Conley, A., Glenn, J., et al. 2014, *ApJ*, **780**, 75
- Duncan, K., Conselice, C. J., Mortlock, A., et al. 2014, *MNRAS*, **444**, 2960
- Dunlop, J. S., McLure, R. J., Biggs, A. D., et al. 2017, *MNRAS*, **466**, 861
- Ellis, R. S., McLure, R. J., Dunlop, J. S., et al. 2013, *ApJL*, **763**, L7
- Endsley, R., Stark, D. P., Charlot, S., et al. 2021a, *MNRAS*, **502**, 6044
- Endsley, R., Stark, D. P., Chevallard, J., & Charlot, S. 2021b, *MNRAS*, **500**, 5229
- Faisst, A. L., Capak, P., Hsieh, B. C., et al. 2016, *ApJ*, **821**, 122
- Faisst, A. L., Capak, P. L., Emami, N., Tacchella, S., & Larson, K. L. 2019, *ApJ*, **884**, 133
- Fazio, G. G., Hora, J. L., Allen, L. E., et al. 2004, *ApJS*, **154**, 10
- Ferland, G. J., Porter, R. L., van Hoof, P. A. M., et al. 2013, *RMxAA*, **49**, 137
- Finkelstein, S. L., Bagley, M., Song, M., et al. 2022, *ApJ*, **928**, 52
- Finkelstein, S. L., Ryan, R. E., Jr., Papovich, C., et al. 2015a, *ApJ*, **810**, 71
- Finkelstein, S. L., Song, M., Behroozi, P., et al. 2015b, *ApJ*, **814**, 95
- Franco, M., Elbaz, D., Béthermin, M., et al. 2018, *A&A*, **620**, A152
- Fudamoto, Y., Oesch, P. A., Schouws, S., et al. 2021, *Natur*, **597**, 489
- Furlanetto, S. R., & Mirocha, J. 2022, arXiv:2208.12828
- Genel, S., Vogelsberger, M., Springel, V., et al. 2014, *MNRAS*, **445**, 175
- Giavalisco, M., Ferguson, H. C., Koekemoer, A. M., et al. 2004, *ApJL*, **600**, L93
- Grazian, A., Fontana, A., Santini, P., et al. 2015, *A&A*, **575**, A96
- Grogin, N. A., Kocevski, D. D., Faber, S. M., et al. 2011, *ApJS*, **197**, 35
- Harikane, Y., Ono, Y., Ouchi, M., et al. 2022, *ApJS*, **259**, 20
- Harikane, Y., Ouchi, M., Shibuya, T., et al. 2018, *ApJ*, **859**, 84
- Hashimoto, T., Laporte, N., Mawatari, K., et al. 2018, *Natur*, **557**, 392
- Hoag, A., Bradač, M., Brammer, G., et al. 2018, *ApJ*, **854**, 39
- Huang, K.-H., Lemaux, B. C., Schmidt, K. B., et al. 2016, *ApJL*, **823**, L14
- Illingworth, G. D., Magee, D., Oesch, P. A., et al. 2013, *ApJS*, **209**, 6
- Inoue, A. K. 2011, *MNRAS*, **415**, 2920
- Ishigaki, M., Kawamata, R., Ouchi, M., et al. 2018, *ApJ*, **854**, 73
- Jiang, L., Kashikawa, N., Wang, S., et al. 2021, *NatAs*, **5**, 256
- Johnson, B. D., Leja, J., Conroy, C., & Speagle, J. S. 2021, *ApJS*, **254**, 22
- Kauffmann, G., Heckman, T. M., Simon White, D. M., et al. 2003, *MNRAS*, **341**, 33
- Kennicutt, R. C., Jr. 1998, *ARA&A*, **36**, 189
- Khusanova, Y., Béthermin, M., Le Fèvre, O., et al. 2021, *A&A*, **649**, A152
- Kikuchihiro, S., Ouchi, M., Ono, Y., et al. 2020, *ApJ*, **893**, 60
- Koekemoer, A. M., Faber, S. M., Ferguson, H. C., et al. 2011, *ApJS*, **197**, 36
- Labbé, I., Bouwens, R., Illingworth, G. D., & Franx, M. 2006, *ApJL*, **649**, L67
- Labbé, I., González, V., Bouwens, R. J., et al. 2010a, *ApJL*, **716**, L103
- Labbé, I., González, V., Bouwens, R. J., et al. 2010b, *ApJL*, **708**, L26
- Labbé, I., Oesch, P. A., Bouwens, R. J., et al. 2013, *ApJL*, **777**, L19
- Labbé, I., Oesch, P. A., Illingworth, G. D., et al. 2015, *ApJS*, **221**, 23
- Labbe, I., van Dokkum, P., Nelson, E., et al. 2022, arXiv:2207.12446
- Lam, D., Bouwens, R. J., Labbé, I., et al. 2019, *A&A*, **627**, A164
- Laporte, N., Meyer, R. A., Ellis, R. S., et al. 2011, *MNRAS*, **505**, 3336
- Larson, R. L., Finkelstein, S. L., Hutchison, T. A., et al. 2022, *ApJ*, **930**, 104
- Leja, J., Carnall, A. C., Johnson, B. D., Conroy, C., & Speagle, J. S. 2019a, *ApJ*, **876**, 3
- Leja, J., Johnson, B. D., Conroy, C., et al. 2019b, *ApJ*, **877**, 140
- Leja, J., Speagle, J. S., Ting, Y.-S., et al. 2022, *ApJ*, **936**, 165
- Liu, D., Daddi, E., Dickinson, M., et al. 2018, *ApJ*, **853**, 172
- Madau, P., & Dickinson, M. 2014, *ARA&A*, **52**, 415
- Mármol-Queraltó, E., McLure, R. J., Cullen, F., et al. 2016, *MNRAS*, **460**, 3587
- Maseda, M. V., Bacon, R., Lam, D., et al. 2020, *MNRAS*, **493**, 5120
- Mawatari, K., Inoue, A. K., Hashimoto, T., et al. 2020, *ApJ*, **889**, 137
- McLeod, D. J., McLure, R. J., & Dunlop, J. S. 2016, *MNRAS*, **459**, 3812
- McLure, R. J., Dunlop, J. S., Cullen, F., et al. 2018, *MNRAS*, **476**, 3991
- Meurer, G. R., Heckman, T. M., & Calzetti, D. 1999, *ApJ*, **521**, 64
- Morishita, T., Trenti, M., Stiavelli, M., et al. 2018, *ApJ*, **867**, 150
- Neistein, E., & Dekel, A. 2008, *MNRAS*, **388**, 1792
- Oesch, P. A., Bouwens, R. J., Illingworth, G. D., et al. 2013, *ApJ*, **773**, 75
- Oesch, P. A., Bouwens, R. J., Illingworth, G. D., et al. 2014, *ApJ*, **786**, 108
- Oesch, P. A., Bouwens, R. J., Illingworth, G. D., Labbé, I., & Stefanon, M. 2018, *ApJ*, **855**, 105
- Oesch, P. A., Brammer, G., van Dokkum, P. G., et al. 2016, *ApJ*, **819**, 129
- Oke, J. B., & Gunn, J. E. 1983, *ApJ*, **266**, 713
- Park, J., Mesinger, A., Greig, B., & Gillet, N. 2019, *MNRAS*, **484**, 933
- Planck Collaboration, Aghanim, N., & Akrami, Y. 2020, *A&A*, **641**, A6
- Rasappu, N., Smit, R., Labbe, I., et al. 2016, *MNRAS*, **461**, 3886
- Roberts-Borsani, G., Morishita, T., Treu, T., Leethochawalit, N., & Trenti, M. 2022, *ApJ*, **927**, 236
- Roberts-Borsani, G. W., Bouwens, R. J., Oesch, P. A., et al. 2016, *ApJ*, **823**, 143
- Roberts-Borsani, G. W., Ellis, R. S., & Laporte, N. 2020, *MNRAS*, **497**, 3440
- Salmon, B., Coe, D., Bradley, L., et al. 2018, *ApJL*, **864**, L22
- Salmon, B., Coe, D., Bradley, L., et al. 2020, *ApJ*, **889**, 189
- Salmon, B., Papovich, C., Finkelstein, S. L., et al. 2015, *ApJ*, **799**, 183
- Salpeter, E. E. 1955, *ApJ*, **121**, 161
- Santini, P., Fontana, A., Castellano, M., et al. 2017, *ApJ*, **847**, 76
- Schaerer, D., & de Barros, S. 2009, *A&A*, **502**, 423
- Schaerer, D., & de Barros, S. 2010, *A&A*, **515**, A73
- Smit, R., Bouwens, R. J., Labbé, I., et al. 2014, *ApJ*, **784**, 58
- Smit, R., Bouwens, R. J., Labbé, I., et al. 2016, *ApJ*, **833**, 254
- Song, M., Finkelstein, S. L., Ashby, M. L. N., et al. 2016, *ApJ*, **825**, 5
- Springel, V., White, S. D. M., Jenkins, A., et al. 2005, *Natur*, **435**, 629
- Stark, D. P., Ellis, R. S., Charlot, S., et al. 2017, *MNRAS*, **464**, 469
- Stark, D. P., Schenker, M. A., Ellis, R., et al. 2013, *ApJ*, **763**, 129
- Stefanon, M., Bouwens, R. J., Illingworth, G. D., et al. 2022a, *ApJ*, **935**, 94
- Stefanon, M., Bouwens, R. J., Labbé, I., et al. 2017, *ApJ*, **843**, 36
- Stefanon, M., Bouwens, R. J., Labbé, I., et al. 2021a, *ApJ*, **922**, 29
- Stefanon, M., Bouwens, R. J., Labbé, I., et al. 2022b, *ApJ*, **927**, 48
- Stefanon, M., Labbé, I., Bouwens, R. J., et al. 2019, *ApJ*, **883**, 99
- Stefanon, M., Labbé, I., Oesch, P. A., et al. 2021b, *ApJS*, **257**, 68
- Stefanon, M., Marchesini, D., Muzzin, A., et al. 2015, *ApJ*, **803**, 11

- Strait, V., Bradač, M., Coe, D., et al. 2020, [ApJ](#), **888**, 124
- Strait, V., Bradač, M., Coe, D., et al. 2021, [ApJ](#), **910**, 135
- Tacchella, S., Bose, S., Conroy, C., Eisenstein, D. J., & Johnson, B. D. 2018, [ApJ](#), **868**, 92
- Tacchella, S., Finkelstein, S. L., Bagley, M., et al. 2022a, [ApJ](#), **927**, 170
- Tacchella, S., Johnson, B. D., Robertson, B. E., et al. 2022b, [arXiv:2208.03281](#)
- Topping, M. W., Stark, D. P., Endsley, R., et al. 2022, [MNRAS](#), **516**, 975
- Walter, F., Decarli, R., Aravena, M., et al. 2016, [ApJ](#), **833**, 67
- Wang, T., Elbaz, D., Schreiber, C., et al. 2016, [ApJ](#), **816**, 84
- Wang, T., Schreiber, C., Elbaz, D., et al. 2019, [Natur](#), **572**, 211
- Weinmann, S. M., Neistein, E., & Dekel, A. 2011, [MNRAS](#), **417**, 2737
- Whitler, L., Stark, D. P., Endsley, R., et al. 2022, [arXiv:2206.05315](#)
- Wilkins, S. M., Bouwens, R. J., Oesch, P. A., et al. 2016a, [MNRAS](#), **455**, 659
- Wilkins, S. M., Feng, Y., Di-Matteo, T., et al. 2016b, [MNRAS](#), **460**, 3170
- Windhorst, R. A., Cohen, S. H., Hathi, N. P., et al. 2011, [ApJS](#), **193**, 27
- Zheng, W., Postman, M., Zitrin, A., et al. 2012, [Natur](#), **489**, 406
- Zheng, W., Zitrin, A., Infante, L., et al. 2017, [ApJ](#), **836**, 210
- Zitrin, A., Labbé, I., Belli, S., et al. 2015, [ApJL](#), **810**, L12